Journal of Applied Phycology
https://doi.org/10.1007/s10811-026-04012-6

RESEARCH

Unravelling the impact of nitrogen deprivation on the morphology and nanomechanical properties of *Parachlorella kessleri*

Alba Zurita[1] · Simona Sebastiano[2] · Jordan Prieto[3] · Jérémy Pruvost[4] · Mariana Titica[4] · Esther Torrens[1] · Cécile Formosa-Dague[2] · Christophe Bengoa[1]

Received: 2 March 2026 / Revised: 24 August 2026 / Accepted: 31 August 2026
© The Author(s) 2026

Abstract

Nitrogen deprivation is commonly applied to enhance lipid accumulation in microalgae for third-generation biofuel production. However, its influence on cell wall morphology and nanomechanical properties, which critically affect downstream processing, remains poorly explored. To address this gap, this study investigated the impact of nitrogen deprivation on these properties of the freshwater microalga *Parachlorella kessleri* using a multi-microscopy approach. Starvation did not lead to any significant morphological changes in either cell size (diameter and height) or cell wall thickness, but it significantly impacted nanomechanical properties: the Young's modulus decreased by approximately 60% (from 1320.7 ± 415.1 to 535.8 ± 346.5 kPa), while surface roughness remained comparable between conditions (1.3 ± 0.5 and 1.9 ± 1.4 nm). Regardless of these similar roughness values, starved cells showed a strong negative correlation between roughness and stiffness, suggesting underlying structural changes not captured by morphology alone. Although biomass freezing for storage and subsequent thawing for analysis may have influenced absolute mechanical values, the comparative trends observed indicate that nitrogen deprivation preconditions the structural and nanomechanical features of this microalga. Therefore, this work highlights the potential of nanomechanical descriptors as complementary indicators for evaluating biomass processability in biofuel and bioproduct applications, opening the door to the development of more efficient and subsequently cost-effective cell disruption strategies.

Keywords *Parachlorella kessleri* · Chlorophyceae · Atomic force microscopy · Force curves · Biofuels · Cell wall · Lipid accumulation

Introduction

The transition towards sustainable energy systems has propelled the development of third-generation biofuels, that aim to overcome the limitations of first- and second-generation biofuels, derived from food crops and lignocellulosic biomass (Mata et al. 2010; Caporgno et al. 2015, 2016). Within this context, microalgae have attracted considerable attention due to their high areal productivity, favourable carbon footprint and potential for integration into circular bioeconomy frameworks (Tibbetts et al. 2015; da Silva Vaz et al. 2016; Sun et al. 2018; Siddiki et al. 2022). However, in spite of decades of research since the first oil crisis in the 1970 s (Spolaore et al. 2006; Mata et al. 2010), the large-scale implementation of microalgal biofuels remains limited by its high production costs, particularly those associated with downstream processing (Caporgno et al. 2015; Dasan et al. 2019).

This bottleneck not only constrains biofuel production, but also limits the development of other microalgae-based products. These photosynthetic microorganisms are rich in a wide range of valuable compounds, including pigments, proteins, lipids, and carbohydrates, whose relative

✉ Christophe Bengoa
christophe.bengoa@urv.cat

[1] Departament d'Enginyeria Química, Universitat Rovira i Virgili, Avinguda Dels Països Catalans 26, 43007 Tarragona, Spain

[2] TBI, Université de Toulouse, INSA, INRAE, CNRS, 31400 Toulouse, France

[3] AlgoSolis, Nantes Université, CNRS UAR3722, 16 Chemin Des Infirmières, 44600 Saint-Nazaire, France

[4] GEPEA, Nantes Université, CNRS, UMR6144, bd de l'Université, CRTT - BP 406, 44602 Saint-Nazaire Cedex, France

Published online: 16 September 2026

abundance strongly depends on their cultivation conditions. Their versatility has promoted the development of innovative approaches to extract and valorise these components (Olkiewicz et al. 2015; Rivas-Navia et al. 2025; Zurita et al. 2025), although microalgal biorefineries (also known as third-generation biorefineries) still face the same challenge: efficient cell disruption.

Downstream processing accounts for approximately 50% of the total costs of microalgae biorefineries (Ruiz et al. 2016; Lam et al. 2018), with cell disruption being one of the most energy-intensive steps (Lee et al. 2010, 2013). This process step is unavoidable, as most target compounds are stored intracellularly. In the case of lipid use for biofuel production, cell lysis is essential, with few exceptions such as *Botryococcus braunii*, which is able to secrete lipids extracellularly (Kemel et al. 2025). Understanding microalgae as biomaterials rather than as purely metabolic systems is thus essential for the rational design of downstream processing strategies, since disruption efficiency is governed by the morphological and mechanical properties of the cells.

In this regard Atomic Force Microscopy (AFM) represents a powerful tool to probe microalgal cells at the nanoscale, enabling the simultaneous characterisation of surface morphology and nanomechanical behaviour (Binnig et al. 1986). Beyond high-resolution imaging, AFM can operate in force spectroscopy mode to generate spatially-resolved maps of mechanical properties from force-distance curves (Cappella and Dietler 1999), all while requiring minimal sample preparation and allowing operation in liquid environments. Despite these advantages, AFM remains underused in microalgal research. According to Demir-Yilmaz et al. (2021), as of 2021, only 49 studies reported AFM application to microalgal systems, highlighting its untapped potential. Most of these works focused on diatoms, even though other classes like Porphyridiophyceae, Trebouxiophyceae, Dinophyceae, Chlorodendrophyceae and Chlorophyceae have also been studied (Mišić Radić et al. 2023). However, only a few used force spectroscopy and, among them, stress-response evaluations were even scarcer (Yap et al. 2016; Novosel et al. 2022a, b; Demir-Yilmaz et al. 2023; Duval et al. 2023), with only one work addressing nutrient deficiency (Yap et al. 2016).

Parachlorella kessleri (formerly known as *Chlorella kessleri* before the taxonomic revision by Krienitz et al. (2004)) is a promising freshwater microalga for biofuel-oriented applications (Taleb et al. 2016, 2018; Kandilian et al. 2019; Heredia et al. 2021), as nitrogen deprivation (i.e., starvation or stress) is commonly applied to redirect metabolism from protein synthesis to triacylglyceride (TAG) accumulation, achieving yields up to 35–40% (Taleb et al. 2018). Regardless of this high lipid content, *P. kessleri* has a particularly robust cell wall, which challenges its lysis and has led to the exploration of a wide range of mechanical disruption techniques, including high-voltage electrical discharges, high-pressure homogenisation, ultrasonication, and bead-milling (Rivera et al. 2018; Villafaña-López et al. 2019; Zhang et al. 2019a, b; Liu et al. 2022).

This work aims to unravel how nitrogen deprivation to boost lipid production preconditions the morphological and nanomechanical properties of *P. kessleri*, focusing on traits that are directly relevant for downstream processing rather than metabolic outputs. Regular and starved cells were studied using a multi-microscopy approach integrating AFM, confocal microscopy, Environmental Scanning Electron Microscopy (ESEM) and Transmission Electron Microscopy (TEM) to evaluate their cell size, cell wall thickness, roughness and Young's modulus. By moving beyond the compositional changes associated with nitrogen deprivation, this study seeks to provide insight into how cultivation strategies influence the mechanical behaviour of the resulting biomass and its susceptibility to disruption. Although *P. kessleri* has previously been examined with AFM in a bioremediation context (Passucci et al. 2024), the different strain origin, cultivation conditions, and large-scale photobioreactor (PBR) and raceway operation employed in the present work clearly differentiate it and reinforce its relevance for industrially-oriented microalgae biorefineries.

Materials and methods

P. kessleri culture and harvesting

Culture medium *Parachlorella kessleri* UTEX 2229 (Austin, Texas, USA) cells were cultivated using modified Bold Basal Medium (BBM), which consisted of (values in mM): 8.820 $NaNO_3$, 0.134 $Na_2EDTA.2H_2O$, 0.913 $MgSO_4.7H_2O$, 0.861 K_2HPO_4, 0.900 KH_2PO_4, 0.035 $CaCl_2.2H_2O$, 0.050 $FeSO_4.7H_2O$, 7.72×10^{-4} $ZnSO_4.7H_2O$, 4.95×10^{-4} $CuSO_4$, 9.15×10^{-3} $MnCl_2.4H_2O$, 0.046 H_3BO_3, 1.51×10^{-4} $Co(NO_3)_2.6H_2O$, 1.06×10^{-3} Na_2MoO_4, 5.000 $NaHCO_3$. When cultivating starved *P. kessleri*, the initial $NaNO_3$ concentration was lowered to 2.3 mM. This nitrate concentration allowed cell proliferation during the initial growth phase until its complete depletion induced nitrogen starvation.

Biomass production The two batches of regular *P. kessleri* were produced in a 40-L indoor column photobioreactor (PBR), at 20ºC maintained through room temperature control, pH maintained at 8.0 via self-regulation through CO_2 injection. Illumination was by artificial light, as depicted in Fig. S1 in the Supporting Information, up to an average photon flux density (PFD) of 300 µmol photons m^{-2} s^{-1}.

This biomass was produced in semi-batch mode to avoid entering into nutrient-limiting conditions. Biomass was accordingly partially harvested, with the remaining cells partially diluted through the addition of fresh BBM, allowing the minimisation of light attenuation. Considering this, it is difficult to define a specific batch duration. The first batch was harvested at day 60 and the second at day 96, and their growth curves can also be found in Fig. S1 (Supporting Information).

In contrast, two different types of cultivation systems were used to produce starved cells: a PBR and a closed raceway, whose pictures can be found in Fig. S2 and S3 (Supporting Information), respectively.

The PBR was a 180-L flat-panel airlift system operated within a greenhouse. Its temperature was kept at 20ºC through a thermoregulated wall, while the CO_2 injection system self-regulated the pH to maintain it at 8.0. This PBR was illuminated with LED panels, whose light intensity was manually-adjusted according to the culture evolution. The PFD was regulated as a function of biomass concentration using the mean rate of photon absorption (MRPA). The MRPA was kept at 13 µmol photons g^{-1} s^{-1} from inoculation until the biomass concentration was approximately 0.85 g L^{-1}. At higher concentrations, the lighting system was not powerful enough to maintain such MRPA, which motivated the setting of a PFD value of 600 µmol photons m^{-2} s^{-1}, the maximum capacity of the lighting system. As a result, the PFD ranged from 100 to 600 µmol photons m^{-2} s^{-1} during the cultivation of starved cells.

The 35-m^2 closed raceway was also operated within a greenhouse environment. This setup also had a thermoregulated floor that kept its temperature at 20ºC, and a pH self-regulation system via CO_2 injection to maintain pH at 8.0. Hoever, cells were cultivated under solar conditions instead.

Both setups for starved *P. kessleri* production operated in batch mode. However, the starvation duration strongly differed. The production in PBR was well standardised, with a duration of 12 days (Fig. S2—Supporting Information) whereas it lasted for 25 days in the raceway (Fig. S3—Supporting Information). This great variation stems from the raceway operation under solar conditions, which makes culture growth strongly dependent on meteorological conditions.

Culture monitoring

In all regular and starved batches, samples were periodically collected during cultivation to monitor cell growth and nutrient progression. Sample collection was conducted using manually-operated valves connected to sampling pipes, discarding the initial volume contained within the pipes to ensure sample representativeness. The concentration of nitrate was frequently tracked with rapid test strips to follow depletion trends, while ion chromatography was used at specific times to evaluate key cations and anions, including nitrates and phosphates. Cell growth was monitored through biomass concentration assessment, and was used as an indicator to ensure harvesting at exponential-late exponential phase in regular cultures and at stationary phase for the nitrogen-starved ones. This biomass concentration tracking enabled the calculation of the specific growth rate, and therefore of the doubling time and the division rate. The expressions to calculate these three parameters can be found in Section S.1. in the Supporting Information.

Biomass harvesting and storage

The harvesting step involved culture transfer from the cultivation systems to a centrifugal decanter with a peristaltic pump (flowrate of ~ 150 L h^{-1} in PBRs, and of ~ 600 L h^{-1} in the raceway). The centrifugal decanter (EVODOS type 10 for the raceway, and DRC30, Rousselet Robatel, France, for the PBRs) operated at around 4000 rpm (4000 rpm, $2700 \times g$ in DRC30; and 4200 rpm, $3000 \times g$ in EVODOS 10) in continuous harvesting mode, allowing the accumulation of biomass in its collection bowl. After shutting down the equipment, biomass with a concentration of approximately 250 g L^{-1} was recovered from the bowl and stored at − 20ºC, a temperature that was also used for sample transportation. All samples underwent identical freezing and thawing procedures prior to analysis, ensuring relative comparisons between biomass types were not affected by sample handling.

Biomass characterisation

Two independent batches of each cultivation condition (regular and starved) were characterised in terms of biochemical composition. The total solids (TS) and total volatile solids (TVS) of wet cells were determined with the standard methods 2540B and 2540E, respectively (Rice et al. 2012). TS were analysed with the Bligh and Dyer (1959) and the Lowry (Lowry et al. 1951) and Dubois (Dubois et al. 1956) methods to quantify lipids, proteins, and carbohydrates, respectively. All analyses for each batch were conducted, at least, in triplicate.

The per-cell dry mass was estimated by dividing the biomass dry weight by the corresponding cell count, which was conducted with a Malassez cell counting chamber.

Reagents for the Bligh and Dyer method: chloroform (ref. 366,927) and methanol (ref. 34,860) were from Sigma Aldrich. Reagents for the Dubois method: D- + -glucose monohydrate ≥ 99.5% (ref. G8270) was supplied by Sigma Aldrich. Sulfuric acid 95–97% (ref. 32,051) was obtained from Honeywell Fluka. Phenol 99.9% (ref. 134,852.1209)

was acquired from Panreac. Reagents for the Lowry method: bovine serum albumin (ref. A9647), copper sulphate pentahydrate (ref. 209,198), Folin-Ciocalteu's phenol reagent (ref. F9252), and sodium tartrate dibasic dihydrate (ref. S4797) were from Sigma Aldrich. Sodium hydroxide (ref. 30,620) was supplied by Honeywell Fluka. Sodium carbonate (ref. 131648.1210) was acquired from Panreac.

Confocal microscopy

Confocal imaging of the two microalgae types was first performed to visually evaluate cell integrity after sample transportation, and also to observe cell autofluorescence and to conduct diameter measurements. A drop of microalgae solution was placed on a poly-L-lysine-coated glass slide (Poly-Prep Slides, Sigma Aldrich) to immobilise the cells before imaging.

The imaging was conducted using a Nikon TE 2000E inverted microscope from the Scientific and Technical Resources Service (SRCiT) of Universitat Rovira i Virgili (URV), using white light and 4 different lasers: red (excitation 633 nm; emission 657/700 nm), green (excitation BP 515–560 nm; emission LP 590 nm), blue (excitation BP 450–490 nm; emission LP 515 nm) and UV (excitation BP 340–380 nm; emission LP 425 nm). Image processing and cell diameter measurements were performed using Image J open-source software, available online at https://imagej.net/. The evaluation of the cell diameter involved the measuring of 100 cells per condition (regular and starved).

Environmental Scanning Electron Microscopy (ESEM)

Environmental Scanning Electron Microscopy (ESEM) is an electronic microscopy technique that allows the imaging of liquid samples thanks to its operation under moderate vacuum. ESEM was used to obtain three-dimensional images to validate AFM imaging results, as AFM is more prone to suffer from resolution problems in bioimaging applications (Wadu-Mesthrige et al. 2001).

To image the two cell types, cells were diluted in their corresponding culture medium, and a drop of the resulting cell solution was pipetted onto a Peltier stage before being transferred into the sample chamber of the equipment (Quanta 600 from FEI Company from the SRCiT of the URV).

Transmission Electron Microscopy (TEM)

Transmission Electron Microscopy (TEM) images were used to verify if the applied stress conditions had led to the accumulation of lipids in the form of granules, and if such stress also induced changes in terms of cell wall thickness.

Sample preparation before imaging (JEOL 1011 from the SRCiT of the URV) can be divided into four major steps: fixation, dehydration, embedding, and sectioning, which were conducted as described in the literature (Zurita et al. 2026). Section S.2. in the Supporting Information explains each of these steps.

Cell wall thickness measurements were done using Image J open-source software. The measurement approach was similar to that described in the literature (Beacham et al. 2014; Yap et al. 2016): for each cell, thickness was measured at five different points, with a total of 12 cells analysed per condition (regular and starved).

Atomic Force Microscopy (AFM)

The imaging and the evaluation of nanomechanical properties of regular and starved cells were conducted with a Bruker Nanowizard IV XP AFM from the Toulouse Biotechnology Institute (TBI). The tip used was a Bruker MLCT non-conductive silicon nitride tip coated with gold and plasma cleaned, with a nominal frequency of 15 kHz, a nominal spring constant of 0.03 N m^{-1}, and a tip opening angle of 17.5°. The spring constant of the cantilever was determined before imaging and force spectroscopy analysis according to the thermal noise method (Hutter and Bechhoefer 1993).

Sample preparation for AFM analysis

50 µL of concentrated biomass was diluted into 10 mL of its corresponding culture medium. The mixture was gently vortexed before dropping 1 mL of this solution on top of poly-L-lysine coated glass slides (Poly-Prep Slides, Sigma Aldrich). The slides were incubated for 30 min before rinsing their surface with the same culture medium to remove non-adhered cells and therefore avoid cell displacement during AFM analysis.

For each culture condition (regular and starved), at least 10 cells from two independent batches were evaluated, following an approach consistent with previous AFM-based studies of microalgal cells (Cvjetinovic et al 2023; Passucci et al. 2024).

AFM imaging and roughness analysis

Height and roughness images were obtained in contact mode using the quantitative imaging mode of the equipment. The applied force was 0.8 nN and the z-length used ranged between 0.5 and 2 µm.

Height images were recorded in 7 × 7 µm areas as *P. kessleri* cell size is typically 2.5 to 10 µm (Takeda 1991; Juárez et al. 2011; Zhang et al. 2019a, b). These images were recorded with a resolution of 120 × 120 pixels. Cell heights

were measured with the AFM software (Bruker, USA) by drawing a line across each individual cell, so cell height was measured as the distance from the baseline (substrate level) to the cell apex (i.e., the maximum height of the topographical profile).

Roughness images were obtained by scanning 1×1 µm areas of the cell surface with a resolution of 150×150 pixels. The data processing software (Bruker, USA) allowed the analysis of these images to obtain the arithmetic average roughness (R_a). The theoretical framework for R_a calculation can be found in Section S.3. in the Supporting Information.

AFM nanomechanical analysis

Nanoindentation experiments were conducted using AFM in force spectroscopy mode, applying forces ranging between 1 and 2.5 nN. 1×1 µm areas on the cell surface were scanned with a resolution of 20×20 pixels, yielding 400 curves per cell. The Hertz-Sneddon contact model (Sneddon 1965) was used to calculate the Young's modulus of each 50 nm indentation curve. Cell incompressibility was assumed by setting 0.5 as the cells' Poisson ratio (Yap et al. 2016; Hsu et al. 2020; Mišić Radić et al. 2022; Novosel et al. 2022a, b; Passucci et al. 2024). The theory behind the calculation of the Young's modulus is detailed in Section S.4. in the Supporting Information.

Statistics and data analysis

Descriptive statistics were used to characterise each morphological and nanomechanical variable for each cell type. Histogram plots were used to visually assess distribution symmetry and relative frequencies in cases where data groups were big ($n \geq 50$), while violin plots combined with individual data point distributions and boxplots provided insights into data density and dispersion in all the evaluated data groups.

The comparisons between regular and starved cells involved the selection of a suitable statistical test. This selection first involved the assessment of normality in each data group using the Shapiro–Wilk test. As the Shapiro–Wilk test is sensitive to big samples ($n \geq 50$), there was an additional study of the impact of the sample size through the Lilliefors (corrected Kolmogorov–Smirnov) test in cases involving big samples.

If samples showed normality, variance homogeneity between groups was evaluated with the Levene's test. This test defined the use of the Welsch's *t*-test (unequal variances) or a standard Student's *t*-test (equal variances) to allow comparison between regular and starved cells. On the other hand, if the Shapiro–Wilk test indicated that one of the data groups did not show normality, a non-parametric Mann–Whitney U test was conducted to compare the two physiological states of *P. kessleri*.

For each microalgae type, it was also evaluated whether there were any statistically significant pairwise correlations between the morphological and nanomechanical parameters obtained from AFM analyses. These correlations were assessed with Spearman's rank correlation coefficient (ρ), which is a non-parametric measure of the strength and direction of the relationship between two values, while statistical significance was evaluated by calculating the corresponding *p*-value.

In all these statistical tests, the significance threshold was set at $p \leq 0.050$, while significance levels were visually indicated in violin plots and correlation matrices with asterisks (* $p \leq 0.050$; ** $p \leq 0.010$; *** $p \leq 0.001$), if applicable (i.e. nothing was indicated if there were no statistically significant differences).

Microsoft Excel was used for descriptive statistics, frequency analysis and histogram preparation. Python (version 3.13) was used for normality evaluation with the Shapiro–Wilk test and its later validation with the Lilliefors (corrected Kolmogorov–Smirnov) test in big samples, variance homogeneity analysis with the Levene's test, as well as *t*-tests and Mann–Whitney U tests (SciPy library). Python was also used to prepare the violin plots with individual data point distributions and boxplots (Seaborn and Matplotlib libraries), as well as the heatmaps with Spearman's correlation coefficients and their corresponding *p*-values (SciPy, Seaborn and Matplotlib libraries).

Results

Stress influence on the growth and biochemical composition of *P. kessleri*

Growth rate monitoring revealed culture-dependent variations. Regular cultures, cultivated in semi-batch mode, had an average specific growth rate of 0.10 ± 0.04 day^{-1} (5 harvest cycles), corresponding to 0.15 ± 0.05 divisions per day. In contrast, starved cells produced in the PBR achieved faster growth rates, 0.33 day^{-1}, while this value went down to 0.08 day^{-1} when cultivated in the raceway. The cell growth of these starved cells decelerated after the exponential phase, as depicted in Fig. S2 and S3 from the Supporting Information. Table S1 in the Supporting Information presents the specific growth rates, doubling times and division rates of each batch.

The effect of nitrogen deprivation on *P. kessleri* was first assessed through compositional analysis. To this end, two independent batches of both regular and starved *P. kessleri* were characterised before conducting morphological and

nanomechanical analyses. The average composition of each biomass type is summarised in Table 1.

The comparisons between regular and starved cells were performed using Student's *t*-test for ashes, lipids and proteins, whereas Welch's *t*-test was applied to carbohydrates due to the unequal variances identified by the Levene's test. While ash content did not differ significantly between conditions ($t(9) = 1.61$, $p = 0.142$), starved cells exhibited a 3.5-fold increase in lipid content ($33.3 \pm 3.2\%$ vs. $9.6 \pm 0.6\%$; $t(12) = -16.34$, $p < 0.001$) along with a 2.6-fold decrease in protein content ($22.3 \pm 2.0\%$ vs. $59.0 \pm 4.1\%$; $t(10) = 19.63$, $p < 0.001$). Carbohydrate levels were also higher in starved cells ($37.3 \pm 10.5\%$ vs. $26.1 \pm 2.4\%$; $t(5.5) = -2.54$, $p = 0.048$), although this increase was associated with substantial inter-batch variability in the starved biomass: the starved batch produced in a PBR had carbohydrate levels comparable to regular cells ($27.8 \pm 1.1\%$), while the one produced in a raceway had remarkably higher values ($46.8 \pm 2.6\%$).

Even with this significant variability in carbohydrate content ($t(4) = -11.89$, $p < 0.001$), both starved batches showed the characteristic metabolic shift associated with nitrogen deprivation, namely lipid accumulation and protein depletion relative to regular cells. Although there were statistically-significant inter-batch differences for both lipid ($34.8 \pm 2.2\%$ vs. $30.2 \pm 2.6\%$; $t(7) = -2.81$, $p = 0.026$) and protein content ($24.1 \pm 0.8\%$ vs. $20.6 \pm 0.6\%$; $t(4) = 5.88$, $p = 0.004$), these differences were less pronounced than those observed for carbohydrates. Minor batch-to-batch differences were also observed in ash content, whereas the two batches of regular cells had consistent compositions ($p > 0.050$ for all components except for ashes). The detailed biochemical composition of each individual biomass batch is provided in Table S2 (Supporting Information).

Table 1 Results of the characterisations of wet *P. kessleri* samples

Ingredient	Regular *P. kessleri*	Starved *P. kessleri*
Total solids, TS (% $w/w_{Biomass}$)	22.4 ± 0.8	22.3 ± 3.7
Moisture (% $w/w_{Biomass}$)[§]	77.6 ± 0.8	77.7 ± 3.7
Ashes (% w/w_{TS})	6.5 ± 1.2 a	5.2 ± 1.6 a
Volatile solids, VS (% w/w_{TS})[֍]	93.5 ± 1.2	94.8 ± 1.6
Carbohydrates (% w/w_{VS})	26.1 ± 2.4 a	37.3 ± 10.5 b*
Lipids (% w/w_{VS})	9.6 ± 0.6 a	33.3 ± 3.2 b***
Proteins (% w/w_{VS})	59.0 ± 4.1 a	22.3 ± 2.0 b***

TS stands for total solids, while VS stands for volatile solids

[§] Calculated by difference with TS

[֍] Calculated by difference with ashes

Values are the average of at least three samples from two independent batches ($n \geq 6$), ± standard deviation

Values with different letters in each row show statistically significant differences ($p \leq 0.050$) according to the Student's *t*-test

Significance levels are indicated with asterisks: $p \leq 0.050$ (*), $p \leq 0.010$ (**), $p \leq 0.001$ (***)

To further characterise the biomass and assess whether freeze–thaw handling affected cell integrity between the two physiological states, per-cell dry mass was estimated from the total solids and cell counts. Regular cells had an average dry mass of 17.6 ± 2.7 pg cell^{-1} ($n = 2$ batches), while this value was 16.3 ± 3.3 pg cell^{-1} ($n = 2$ batches) in starved cells. Indeed, in spite of the inter-batch differences observed in compositional terms, none of the morphological or nanomechanical descriptors showed significant inter-batch variation. Therefore, the following sections present results comparing the two biomass types as a whole, without explicitly considering inter-batch variability.

Stress influence on the size of *P. kessleri*

The size differences between nitrogen-deprived (starved) and regular *P. kessleri* were evaluated in terms of cell diameter and cell height. The results that were obtained are described in the subsections below.

Cell diameter

As previously indicated, the cell diameter was evaluated using confocal microscopy images by measuring 100 cells per condition (regular and starved). Figure 1 exemplifies the type of images obtained for both types of cells with the confocal microscope: white field and chlorophyll fluorescence. As can be seen, both cell types were circular, although some exhibited slight deformation. Autofluorescence was high under green light excitation, as presented in panels c and d of Fig. 1. However, in the starved batch there were some oval-like shapes that presented no autofluorescence, which were inferred to be cell debris.

The normality in data distributions was assessed using the Shapiro–Wilk test, which confirmed that the sizes of starved cells did not significantly deviate from a normal distribution ($W = 0.98$, $p = 0.083$), while those of regular cells did ($W = 0.96$, $p = 0.004$). As this test is sensitive to big samples, the Lilliefors test was applied as a validation, confirming the deviation from normality of the regular sample ($D = 0.11$, $p = 0.009$) as well as normality in the starved one ($D = 0.08$, $p = 0.090$). Given that normality assumptions were not met for one of the groups, the Mann–Whitney U test was used to evaluate the differences between these two physiological conditions. This test revealed no statistically significant differences between regular and starved cells ($U = 5735.50$, $p = 0.073$), indicating that nitrogen deprivation did not significantly impact the cell diameter of *P. kessleri*.

This observation explained why the average cell diameter was practically identical between these two cell types: 5.7 ± 1.4 µm and 5.4 ± 1.4 µm for regular and starved cells, respectively. These similarities also extended to the minimum and maximum cell sizes: 3.0–9.6 µm for regular cells and

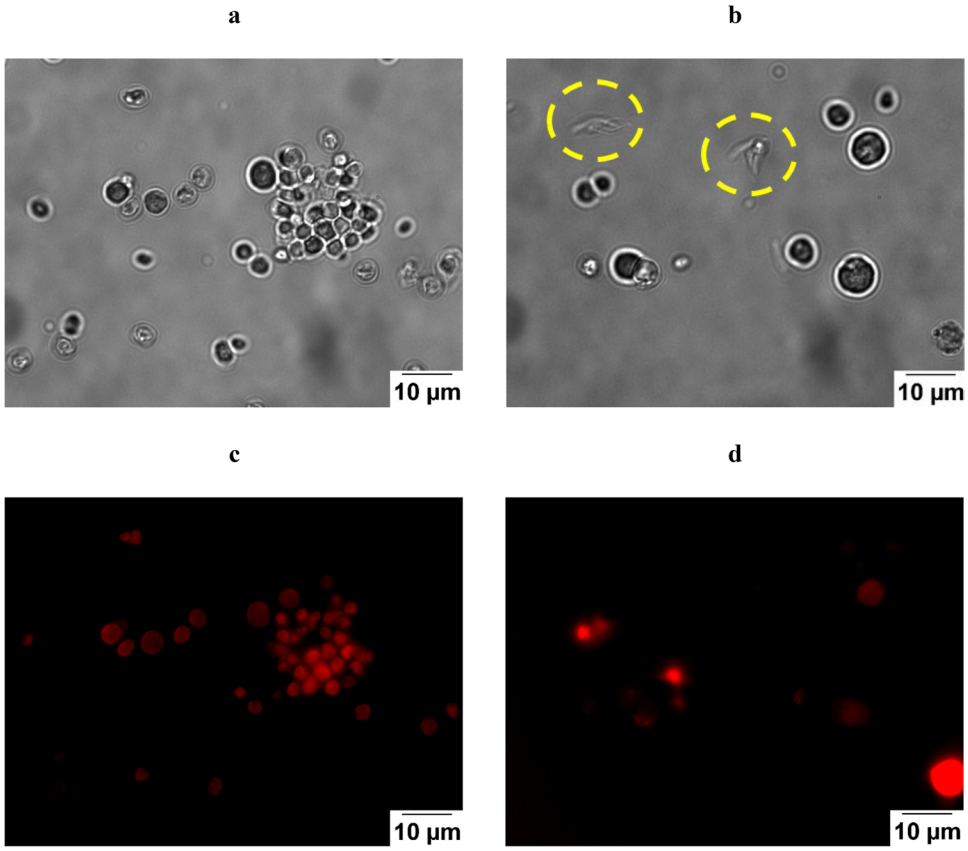

Fig. 1 Confocal microscopy images from regular (**a**, **c**) and starved (**b**, **d**) *P. kessleri* cells. Panels a and b correspond to the bright field image (white light excitation), while c and d correspond to chlorophyll fluorescence (green excitation). The yellow circles with dashed contours in panel b indicate the presence of cell debris

2.5–9.2 µm for starved cells. Full descriptive statistics for cell diameters can be found in Table S3 (Supporting Information).

The differences between the two cell types can be visually observed in Fig. 2 in the form of histograms in panel a and violin plots in panel b. The frequency tables prepared for histogram construction can be found in Tables S4 and S5 (Supporting Information).

These average cell diameters along with the per-cell masses allowed the calculation of the apparent cell density, which was 0.18 pg μm^{-3} for regular cells and 0.20 pg μm^{-3} for the starved ones.

Cell height

Cell height evaluation for both physiological states of *P. kessleri* was conducted using AFM micrographs. As depicted in Fig. 3, both cell types exhibited comparable average heights: 2.6 ± 0.5 µm in regular cells and 2.8 ± 0.6 µm in starved cells, although their distributions were different. The distribution of regular cells had some asymmetry with a slight leptokurtosis, while that of starved cells was near-symmetric and more platykurtic. Complete descriptive statistics for cell heights are provided in Table S6 (Supporting Information).

Normality was evaluated with the Shapiro–Wilk test, which indicated normality only for the starved cell dataset ($W = 0.90$, $p = 0.083$), while regular cells deviated significantly from normality ($W = 0.88$, $p = 0.005$). Consequently, the two groups were compared using the Mann–Whitney U test, which confirmed that nitrogen starvation did not significantly affect the cell height of *P. kessleri* ($U = 186.50$, $p = 0.262$).

Stress influence on the internal morphology of *P. kessleri*

As shown in the previous section, nitrogen deprivation did not lead to any statistically significant differences in cell size. Hence, the next step was to evaluate how stress affected the internal morphology of *P. kessleri*.

TEM images confirmed lipid accumulation in starved cells, which exhibited large lipid bodies, as shown in Fig. 4 (additional TEM micrographs for regular and starved cells can be found in Fig. S4 and S5, respectively, in the Supporting Information). Beyond visualising lipid body accumulation, TEM micrographs were used to evaluate cell wall thickness, which was very similar between the two cell types. The average cell wall thickness was 71.6 ± 11.0 nm for regular cells and 75.3 ± 16.0 nm for starved cells. Full descriptive statistics can be found in Table S7 (Supporting Information). The distribution of cell wall thicknesses is represented as histograms and violin plots in Fig. 5 (panels a and b, respectively). The frequency distribution tables

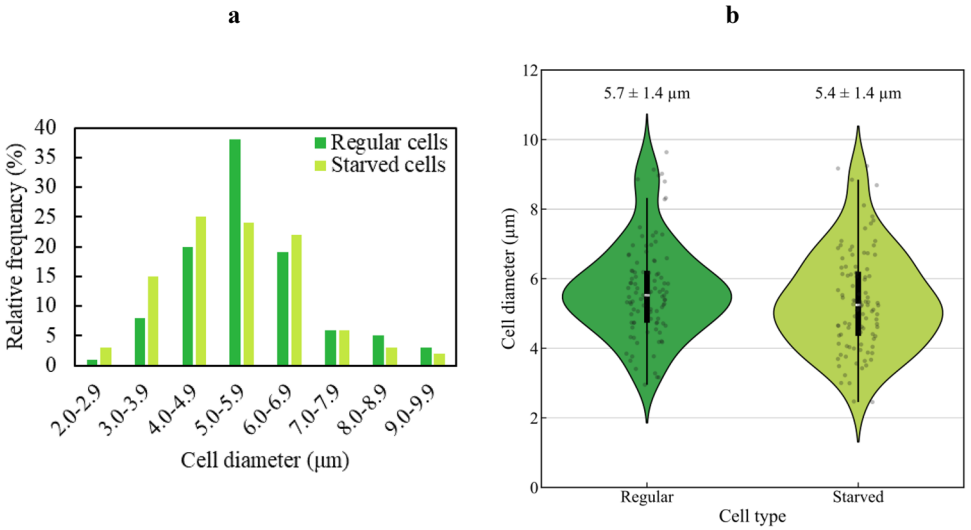

Fig. 2 Comparison of cell diameter between regular and stressed *P. kessleri* cells. Panel a presents histograms and b violin plots with integrated boxplots and the dispersion of the different datapoints. The white line on the boxplot represents the median. Both plots have been constructed with 100 measurements for each cell type ($n = 100$). Significance levels are indicated with asterisks: $p \leq 0.050$ (*), $p \leq 0.010$ (**), $p \leq 0.001$ (***). The absence of asterisks indicates that the difference between groups was not statistically significant. Average values and their standard deviations are presented on top of each individual violin plot

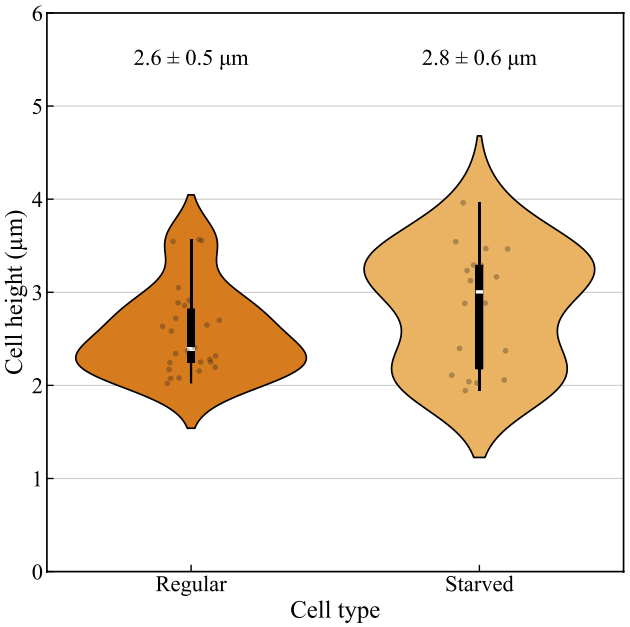

Fig. 3 Comparison of cell heights between regular ($n = 26$) and starved ($n = 18$) *P. kessleri* cells with violin plots with integrated boxplots and the dispersion of the different datapoints. The white line on the boxplots represents the median. Significance levels are indicated with asterisks: $p \leq 0.050$ (*), $p \leq 0.010$ (**), $p \leq 0.001$ (***). The absence of asterisks indicates that the difference between groups was not statistically significant. Average values and their standard deviations are presented on top of each individual violin plot

used to build these histograms are available in Tables S8-S9 (Supporting Information). Both distributions were near-symmetrical and mesokurtic, reinforcing the similarity between the two cell types.

The normality of each group of data was studied with the Shapiro–Wilk test. Unlike cell size evaluation, the cell wall thicknesses of regular cells presented a normal distribution ($W = 0.99$, $p = 0.916$) while starved cells did not ($W = 0.95$, $p = 0.013$). Due to the test sensitivity to big samples, the Lilliefors test was used to confirm such observations, doing so for both regular ($D = 0.06$, $p = 0.789$) and starved ($D = 0.12$, $p = 0.046$) cells. The two types of cells were accordingly compared with the Mann–Whitney U test, which revealed no statistically significant differences between them ($U = 1641.00$, $p = 0.405$). This result further confirmed that stress did not substantially impact *P. kessleri*.

Stress influence on the cell surface properties of *P. kessleri*

This section dives deep into nitrogen deprivation impact on two surface properties of *P. kessleri*: roughness and Young's modulus. Both properties were quantitatively determined through AFM analyses.

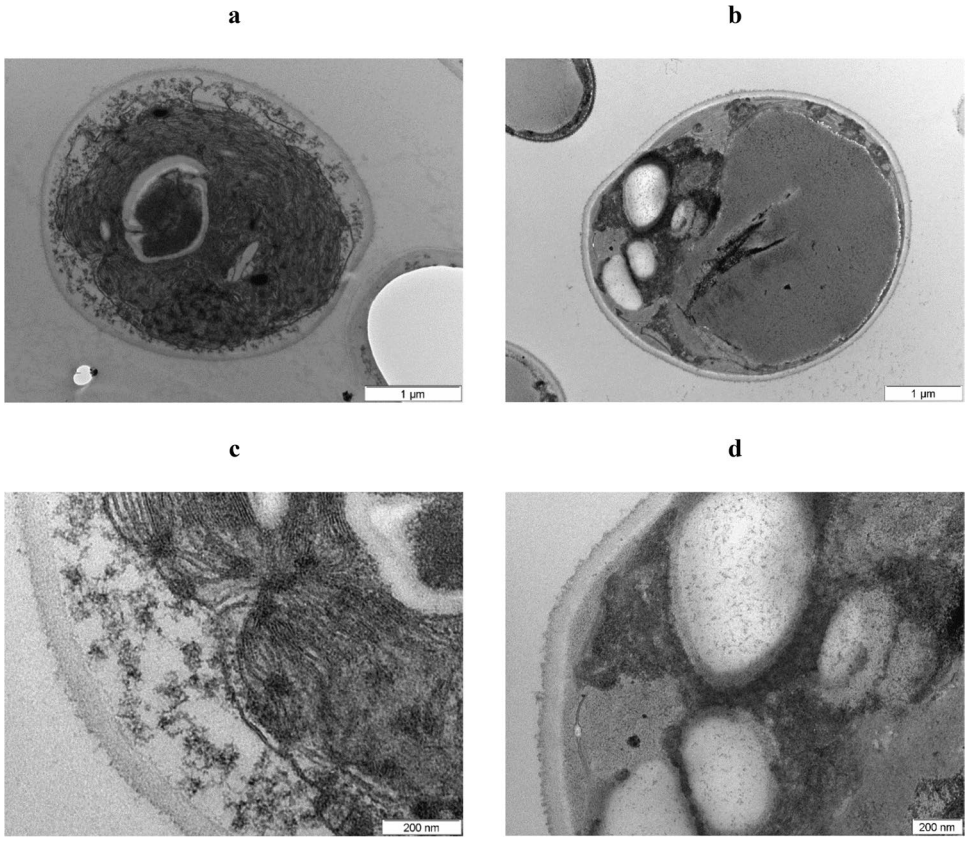

Fig. 4 TEM images obtained from regular (**a**, **c**) and starved (**b**, **d**) *P. kessleri* cells. Panels a and b present a general view of a single cell, while panels c and d show the cell wall in more detail. The large dark granules in the starved cell are lipid bodies, while the white ones correspond to starch granules, which can also be seen in the regular *P. kessleri* cell (although they are smaller)

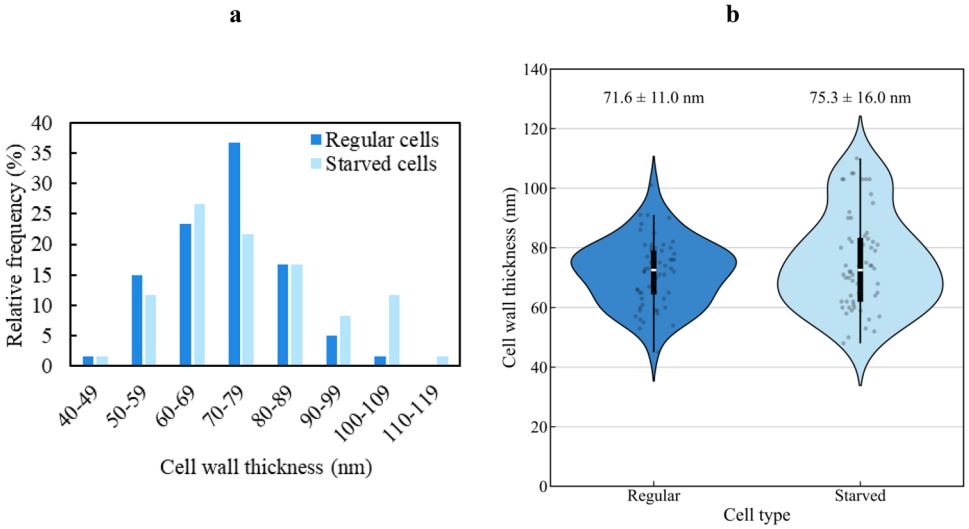

Fig. 5 Comparison of cell wall thicknesses between regular and starved *P. kessleri* cells. Panel a presents histograms and b violin plots with integrated boxplots and the dispersion of the different datapoints. The white line on the boxplot represents the median. Both plots have been constructed with 60 measurements for each cell type ($n = 60$). Significance levels are indicated with asterisks: $p \leq 0.050$ (*), $p \leq 0.010$ (**), $p \leq 0.001$ (***). The absence of asterisks indicates that the difference between groups was not statistically significant. Average values and their standard deviations are presented on top of each individual violin plot

Cell roughness

ESEM micrographs allowed the visualisation of the cell wall surface of *P. kessleri*, validating the sphere-like geometries observed in the confocal and AFM micrographs used for cell size measurements.

Figure 6 displays a series of ESEM images of both cell types, whose surfaces looked very smooth despite punctual inhomogeneities. As this microscope allows operation with wet samples, which requires partial vacuum, these conditions may have led to the collapse of some cells.

While ESEM imaging suggested relatively smooth surfaces in both cell types, AFM analysis provided the nanoscale resolution necessary to detect and quantify subtle roughness differences that were not apparent at the microscale level. AFM roughness analysis went beyond these ESEM observations, recording cell topography images in 1 μm × 1 μm areas on top of the cells to quantify roughness, as can be seen in Fig. 7.

As with morphological attributes, the two cell types showed similar roughness values, which were 1.3 ± 0.5 nm in regular cells and 1.9 ± 1.4 nm in the starved ones. Complete descriptive statistics can be found in the Table S10 (Supporting Information).

The violin plots in Fig. 8 illustrate that the average roughness distribution in regular cells was compact, with a slight right-skew and moderately heavy tails. In contrast, the distribution for starved cells was more elongated, with stronger right-skewness and markedly heavy tails, describing an asymmetric and leptokurtic profile.

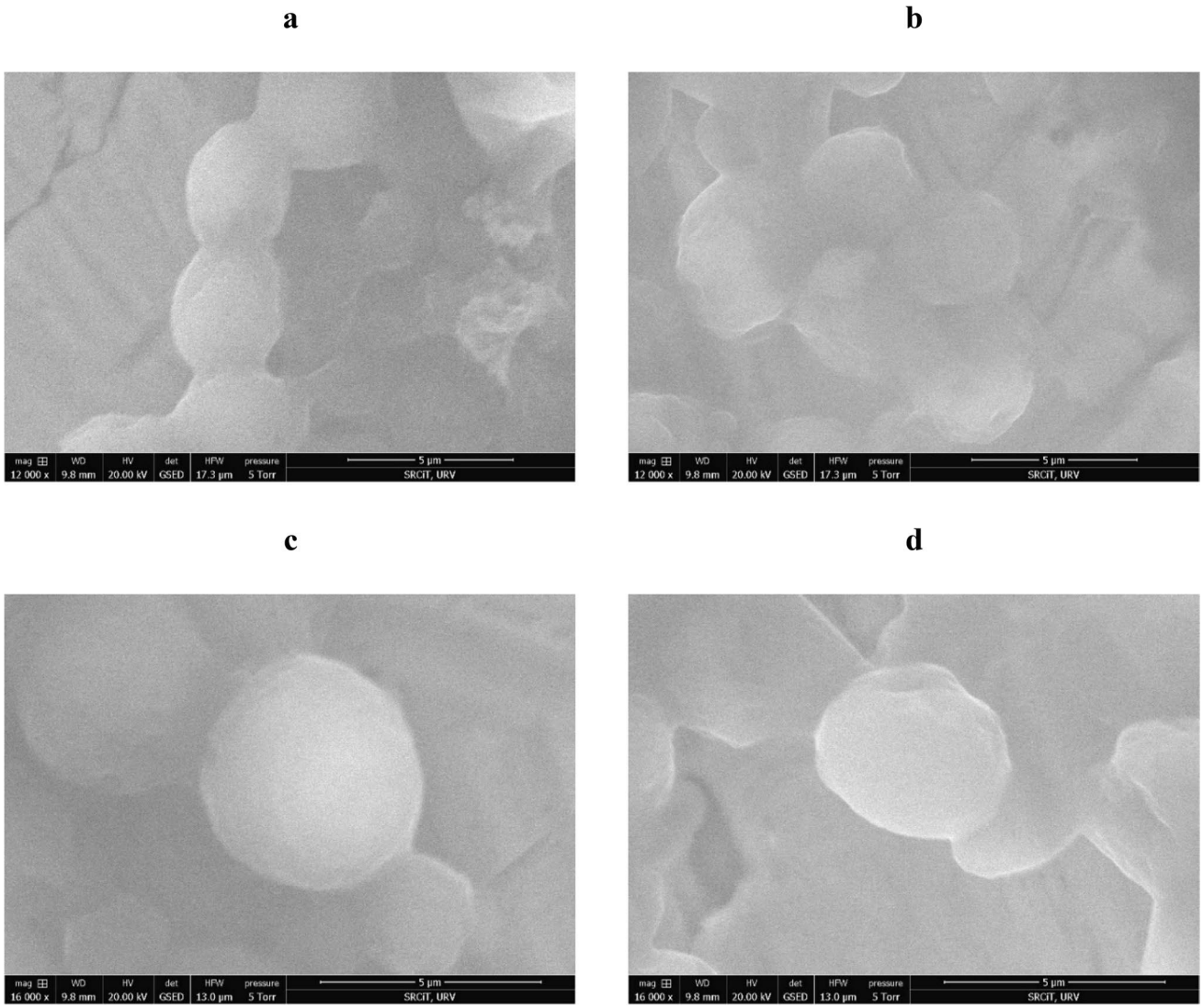

Fig. 6 ESEM images obtained from regular (**a**, **c**) and starved (**b**, **d**) *P. kessleri* cells. Panels a and b show a series of cells, while panels c and d show a detail of a single cell. The lines that appear in the background of these images do not belong to the samples, but to the Peltier stage that supported them

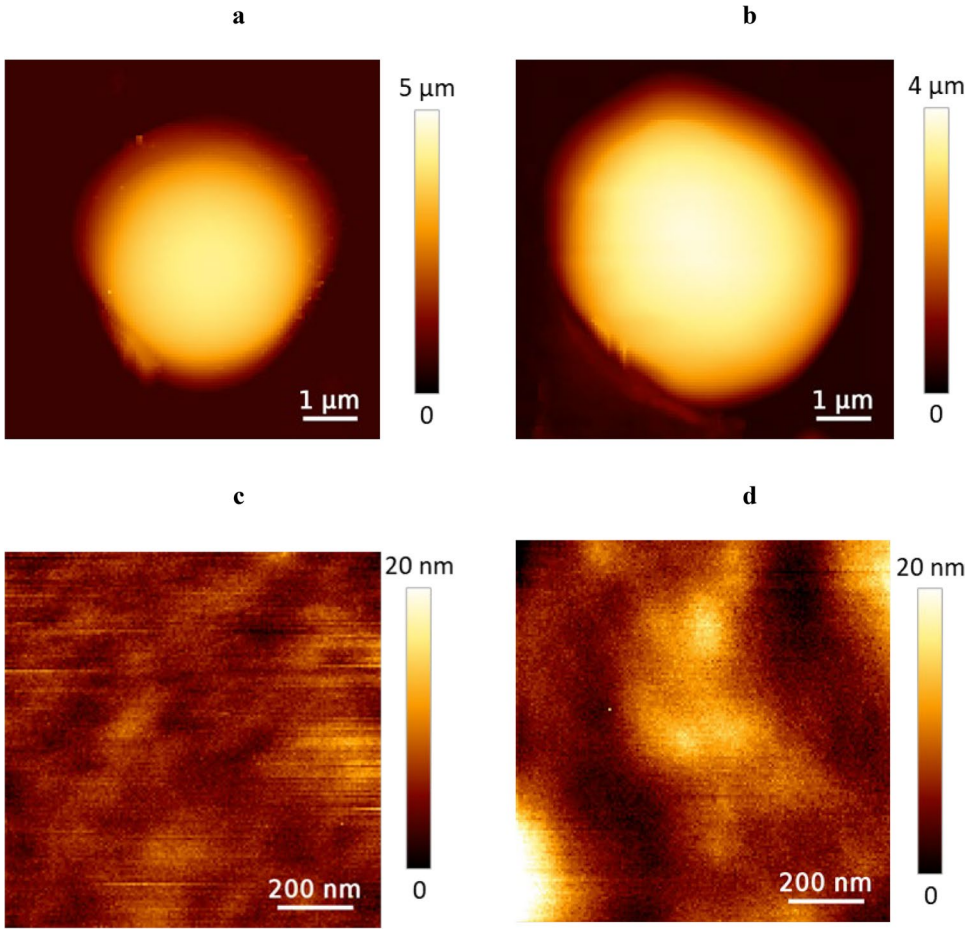

Fig. 7 AFM images obtained from regular (**a**, **c**) and starved (**b**, **d**) *P. kessleri* cells. Panels a and b present a high-resolution image of a cell in a 7 µm × 7 µm area, while panels c and d show 1 µm × 1 µm areas scanned for roughness analysis on top of those cells

The Shapiro–Wilk test confirmed a strong deviation from normality in both cell types ($W = 0.78$, $p < 0.001$ for regular cells and $W = 0.66$, $p < 0.001$ for the starved ones), which subsequently motivated the use of the Mann–Whitney U test for their comparison. This test revealed, once more, no statistically significant differences ($U = 123.00$, $p = 0.065$), showing that nitrogen deprivation did not significantly affect the cell surface roughness of *P. kessleri*.

Young's modulus

Force spectroscopy analysis explored the stress-induced changes in microalgal elasticity. Figure 9 shows the Young's modulus distribution for regular and starved cells, comprising all recorded values (panel a) and the per-cell averages (panel b). For consistency purposes and to avoid pseudoreplication, statistical analyses were performed only on the average values.

The average Young's modulus of regular cells was 1320.7 ± 415.1 kPa, which was about 2.5 times higher than the value recorded in starved cells, 535.8 ± 346.5 kPa. Full descriptive statistics can be found in the Table S11 (Supporting Information). The Shapiro–Wilk test revealed data normality for both groups ($W = 0.93$, $p = 0.116$ for regular cells and $W = 0.90$, $p = 0.072$ for the starved ones), so the homogeneity of variances was verified with Levene's test ($W = 0.03$, $p = 0.855$), supporting the application of a Student's *t*-test under the assumption of equal variances. The test confirmed a very significant difference between groups ($t(35) = 6.11$, $p < 0.001$), demonstrating the impact of nitrogen deprivation on the nanomechanical properties of the *P. kessleri* cell wall. Given the relatively small sample sizes ($n = 21$ for regular cells and $n = 16$ for the starved ones), a Mann–Whitney U test was additionally performed as a conservative non-parametric alternative. This test corroborated the results of the parametric analysis ($U = 314.00$, $p < 0.001$), further validating the robustness of the findings.

Evaluation of parameters' interaction for each cultivation condition

AFM data underwent further evaluation to discern whether there were any correlations between morphological and nanomechanical properties for each cultivation condition. Each group was accordingly studied using the non-parametric Spearman's rank correlation coefficients (ρ) and their

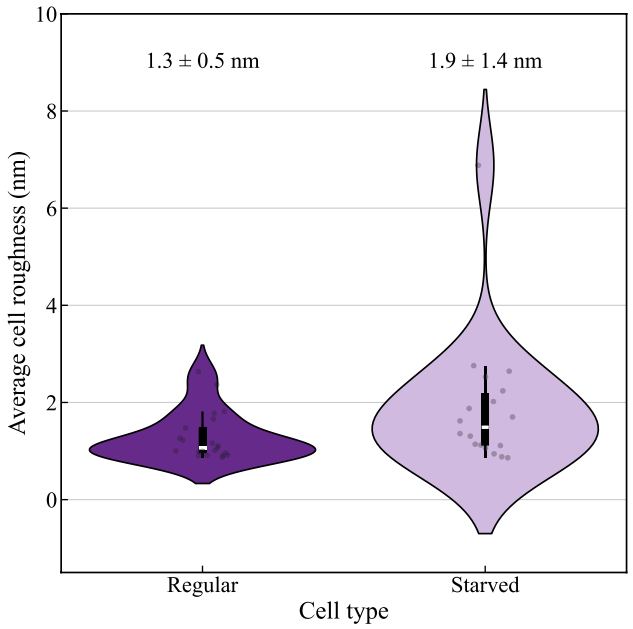

Fig. 8 Comparison of average cell roughness between regular ($n=21$) and starved ($n=18$) *P. kessleri* cells with violin plots with integrated boxplots and the dispersion of the different datapoints. The white line on the boxplots represents the median. Significance levels are indicated with asterisks: $p \leq 0.050$ (*), $p \leq 0.010$ (**), $p \leq 0.001$ (***). The absence of asterisks indicates that the difference between groups was not statistically significant. Average values and their standard deviations are presented on top of each individual violin plot

corresponding *p*-values to identify their interactions. The correlation matrices in Fig. 10 present Spearman's ρ values in the lower triangle, while *p*-values are plotted in the upper one. The tables with the cell diameter, cell height, average roughness and average Young's modulus for each individual cell for each cultivation condition used for this study can be found in Tables S12-S13 (Supporting Information).

The only correlation identified for regular cells was that smaller diameters correlated with increased rigidity ($\rho=-0.70$, $p=0.003$). However, two more elements reached *p*-values very close to the significance threshold: the positive correlation between cell diameter and height ($\rho=0.45$, $p=0.082$) and the negative one between cell height and average Young's modulus ($\rho=-0.44$, $p=0.085$). The other possible interactions between factors in regular cells fell far from statistical significance. This was the case of both cell diameter and height with the average roughness ($p=0.572$ and $p=0.953$, respectively), indicating that they were essentially independent from each other. The average roughness and average Young's modulus interaction was also not significant, but not as much as the two previous combinations ($p=0.141$).

In contrast, the height-diameter interaction was very strong and positive in starved cells ($\rho=0.82$, $p<0.001$), highlighting their spherical nature, and the interaction between average Young's modulus and average roughness was statistically significant, revealing that softer cells had rougher surfaces ($\rho=-0.77$, $p=0.001$). As for the remaining pairwise

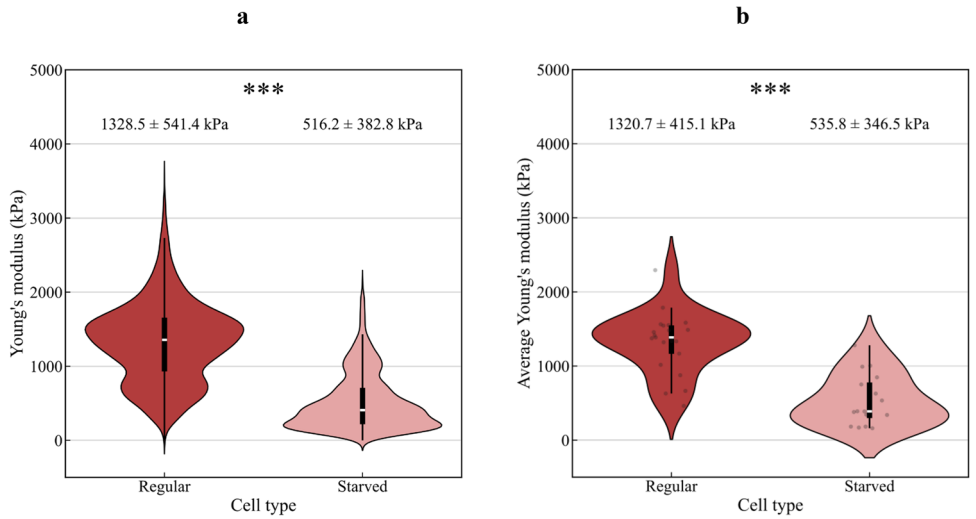

Fig. 9 Comparison of Young's modulus between regular and starved *P. kessleri* cells with violin plots with integrated boxplots. The white line on the boxplots represents the median. Panel a is the comparison including all the recorded values for each cell type ($n>5500$) while panel b just comprises the average Young's modulus ($n_{regular}=21$, $n_{starved}=16$). Panel b also shows the dispersion of the different datapoints, which was not included in panel a for clarity purposes. Significance levels are indicated with asterisks: $p \leq 0.050$ (*), $p \leq 0.010$ (**), $p \leq 0.001$ (***). The absence of asterisks indicates that the difference between groups was not statistically significant. Average values and their standard deviations are presented on top of each individual violin plot

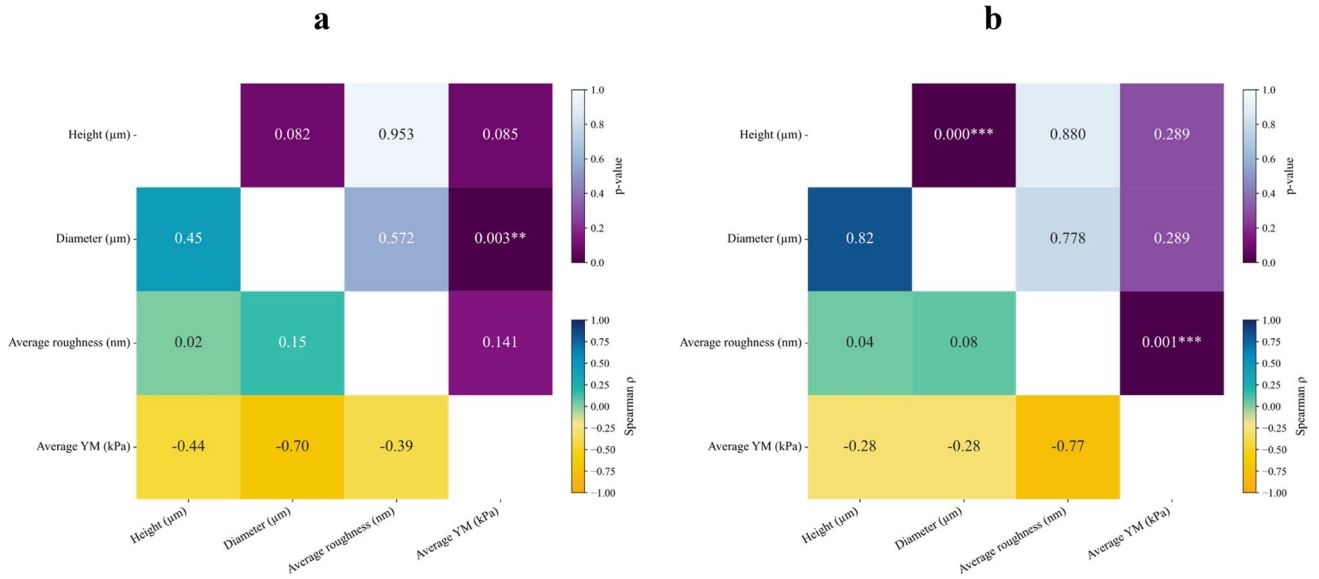

Fig. 10 Heatmaps representing Spearman's rank correlation coefficients (ρ) in the lower triangle and their corresponding p-values in the upper triangle, describing the relationships between cell height, diameter, average roughness and average Young's modulus (YM) in regular (**a**) and starved (**b**) *P. kessleri* cells. Significance levels are indicated with asterisks: $p \leq 0.050$ (*), $p \leq 0.010$ (**), $p \leq 0.001$ (***). The absence of asterisks in some matrix cells indicates that the interaction was not statistically significant. A Spearman's ρ equal to 1 means there is a perfect positive correlation between the two factors (i.e. both increase together), a Spearman's ρ equal to -1 indicates a perfect negative correlation (i.e. when one increases the other decreases), while a Spearman's ρ equal to 0 indicates that there is no detectable correlation

interactions, all of them presented mild or low Spearman's ρ, but none of them passed the significance threshold.

Discussion

This study explored the impact of nitrogen deprivation on *P. kessleri* by moving beyond the well-characterised metabolic response to examine how this stress preconditioned cell morphology and nanomechanical properties relevant to downstream processing. The results for each of the assessed parameters are discussed in the sections below.

Biochemical and per-cell mass response to nitrogen deprivation

The biochemical composition data in Table 1 confirmed the expected metabolic shift associated with nitrogen deprivation: a 3.5-fold increase in lipid content (from 9.6 to 33.3%) and a 2.6-fold decrease in protein content (from 59.0 to 22.3%), consistent with previous reports for *P. kessleri* under similar conditions (Taleb et al. 2016, 2018; Kandilian et al. 2019). The substantial inter-batch variability in carbohydrate content of starved batches (27.8% for the PBR batch and 46.8% for the raceway) reflected the dynamic nature of starch accumulation during nitrogen deprivation: nutrient deficiency initially triggers starch production, which is later degraded to facilitate lipid biosynthesis for long-term starvation (Ran et al. 2019). In spite of this compositional heterogeneity, both starved batches were clearly differentiated from regular cells, confirming effective nitrogen deprivation in both cultivation systems.

Regular and starved batches had comparable per-cell dry masses (17.6 ± 2.7 pg cell^{-1} and 16.3 ± 3.3 pg cell^{-1}, respectively) aligned with the 6.36—22.4 pg cell^{-1} reported for *Chlorella vulgaris* (Hu 2014; Fekete et al. 2024), indicating that nitrogen deprivation triggered a compositional redistribution rather than a net change in the total cellular biomass. In fact, the slightly higher apparent density of starved cells is consistent with the replacement of less dense cytoplasmic proteins by denser lipid bodies or starch granules (Wang et al. 2009). Still, the presence of cell debris in starved cell images (Fig. 1a) suggests that freeze–thaw handling along with the mechanical weakening induced by nitrogen deprivation (60% reduction in Young's modulus) may have compromised the integrity of some cells. The preservation of similar average cell masses across physiological states indicates that this fragilisation was not extensive enough to cause a measurable loss of total biomass, but rather affected some cells that were already structurally compromised by starvation. This interpretation is consistent with the roughness-softness correlation observed in starved cells (see the Results section "Evaluation of parameters' interaction for each cultivation condition"), which points to surface degradation processes

that could predispose cells to mechanical failure during freeze–thaw cycles. Some AFM studies on microalgae have shown how surface morphological changes reflect underlying structural modifications that affect cellular mechanical properties (Shu et al. 2017; Mišić Radić et al. 2022). The lack of this correlation in regular cells subsequently suggests that, under regular cultivation conditions, the mechanical properties of the cell wall are independent from their surface topology.

External and internal cell morphology under nitrogen deprivation

Contrary to expectations from the broader microalgae literature, nitrogen deprivation did not significantly alter the diameter, height, and cell wall thickness of *P. kessleri*.

As depicted in Fig. 1, regular and starved cells showed high autofluorescence under green light excitation, which corresponds to chlorophyll *a* absorption (Kautsky and Hirsch 1931; Raven and Beardall 2006), and were circular, yet some were slightly deformed. These minor deformations probably stemmed from the freezing and thawing of the samples, which has been reported to induce morphological changes in microalgae (Abreu et al. 2012).

Cell heights were very similar across microalgae types, and so were their diameters, which were aligned with values reported for *P. kessleri* in other works (Takeda 1991; Juárez et al. 2011; Zhang et al. 2019a, b). However, cell height values were lower than the diameter ones even though *P. kessleri* is considered spherical (Krienitz et al. 2004). This discrepancy stems from the combined effect of spreading and slight flattening that cells experience when adhered to adhesive substrates (in this case, poly-L-lysine), which may have induced some deformation (Pietuch and Janshoff 2013; Godon et al. 2017), although the force exerted by the AFM tip may have also had some impact (Rheinlaender et al. 2020). In any case, the height-diameter interaction was very strong and positive in starved cells ($\rho = 0.82$, $p < 0.001$), and was also positive and very close to statistical significance in regular cells ($\rho = 0.45$, $p = 0.082$), confirming that the discrepancies between cell diameters and heights reflected morphological differences rather than measurement artefacts. The cell wall thickness values of the two types of *P. kessleri* cells were also very similar, and were aligned with those reported in the literature for other members of the Chlorellaceae (Yap et al. 2016; Spain and Funk 2022).

Returning to the comparison across physiological states, the lack of statistically significant differences in terms of cell size and cell wall thickness contrasts with results reported in other studies on the impact of nutrient stress on microalgae morphology. In those publications, nitrogen deprivation or limitation led to larger cell sizes as well as to an increase in cell wall thickness (Shivakumar et al. 2024). For example, Yap and co-workers (2016) evaluated the impact of nitrogen deprivation on *Nannochloropsis* sp., *Chlorella* sp. and *Chlorococcum* sp. In all cases, nitrogen-deprived cells experienced an increase in size, which was of 25% in *Nannochloropsis* sp. and *Chlorococcum* sp., and 20% in *Chlorella* sp., as well as statistically significant cell wall thickening. In the case of *Chlorella* sp., the closest species to *P. kessleri*, the cell wall thickness went from 52 ± 19 nm in regular conditions to 88 ± 17 nm under nitrogen deprivation conditions. Similarly, in the work by Jeong et al. (2017), the group observed how the cell wall of nitrogen-limited *Nannochloropsis salina* was 1.54 times thicker than in nitrogen-repleted cells, which was caused by the apparent swelling of the inner cell layer. Regarding *Tetradesmus* species, Chokshi et al. (2017) studied the impact of nitrogen starvation on *Tetradesmus dimorphus*, reporting that cells doubled in length and slightly increased in width after just one day of starvation, while Pancha et al. (2014) observed how *Tetradesmus obliquus* moderately increased in size and transitioned from unicellular forms to 2- or 4-cell coenobia with spines at terminal cells under nitrate-limited conditions. The rationale behind these changes in starved cells was explained by Halim and his colleagues (Halim et al. 2019). In their work, they tracked the cell volume and cell wall thickness evolution of *Nannochloropsis* sp. cells in relation to nitrogen availability, whose content progressively decreased to induce cell starvation. After four days, cells had a big volume as they formed binary fission complexes. However, as the nitrogen deprivation onset approached, cell division slowed down and the cell volume decreased, reaching the smallest value on day fourteen. Conversely, on day twenty-eight, cells were bigger, as they had expanded due to the accumulation of lipid bodies. Regarding the cell wall, they did not observe much variance during the fourteen days that the growth phase lasted for. However, when nitrogen deprivation began, cells experienced a substantial cell wall thickening as the carbon flux of the cell went from photosynthetic routes to the synthesis of structural polysaccharides. Roncaglia and her colleagues (2021) also observed a slight but statistically significant increase in the cell wall thickness in nitrogen-starved *Nannochloropsis oceanica* F&M-M24 (32.9 nm in repleted cells and 37.8 nm in starved cells). In this case, this increase was at the expense of the number of cell wall layers, as nitrogen-repleted cells had two while the starved ones just one.

Other types of stress have also been reported to induce cell size changes in microalgae. For instance, cultivation in cold water led to an increase in cell diameter during both the exponential and stationary phases of *Haematococcus pluvialis*, *Chlorella vulgaris* sp. and *Scenedesmus* sp., whereas *Coelastrella* sp. cells did not grow at this lower temperature (González-Hourcade et al. 2023). Nevertheless, it must be noted that not all forms of stress necessarily lead to an

increase in cell size or cell wall thickness. For example, different combinations of salinity, pH and temperature can lead to cell size increases as well as decreases, as reported in the work by Bautista-Chamizo and her team (2018) with *Phaeodactylum tricornutum*, whereas high salinity has led to decreases in the cell wall thickness of *N. salina* (Beacham et al. 2014). Therefore, cellular responses to stress can vary greatly among microalgal species.

The reason why *P. kessleri* kept a stable size and cell wall thickness under nitrogen deprivation could stem from several factors. First, the starvation conditions applied (duration and/or severity) may have been insufficient to trigger a morphological response to stress. Second, this cell size increase and cell wall thickening response seems to be species-specific, as evidenced by the differences reported across microalgal species in the literature. And third, this strain may have a low degree of morphological plasticity and may prioritise alternative stress response strategies under nitrogen deprivation, such as lipid accumulation for energy storage or cell wall composition changes rather than its thickening.

This lipid storage in *P. kessleri* is evidenced in Fig. 4 as well as the additional images available in the Supporting Information (Fig. S4 and S5). These lipid granules are the result of a metabolic shift from protein synthesis to TAG production and storage (as shown in Table 1), triggered by the absence of nitrogen, which makes cells prioritise energy storage over division and growth (Rodolfi et al. 2009; Breuer et al. 2012; Taleb et al. 2018). In addition to this, nitrogen deprivation leads to a reduction in the chlorophyll content of the cells, which decreases their photosynthetic activity (Pruvost et al. 2009, 2011) and ultimately alters their colouration, with nitrogen-replete cells looking green and starved cells exhibiting a yellowish hue, as can be seen in Fig. S1-S3 in the Supporting Information.

Besides stress, the division rate of microalgal cells can also influence their size (Concas et al. 2016), as often, faster growing cultures lead to smaller cells (Filali et al. 2021). In the present work, cell growth kinetics differed across cultivation conditions: 0.10 ± 0.04 day^{-1} (5 harvest cycles) in regular cells, 0.33 day^{-1} in starved cells cultivated in the PBR, and 0.08 day^{-1} in starved cells cultivated in the raceway, respectively. This stark variation between starved batches reflects the strong impact of process-intensified and solar conditions on cell growth kinetics. Still, no changes in cell size were observed despite these differences in growth kinetics, as each cell type was harvested at the same growth phase (Havlik et al. 2013; Duval et al. 2023).

Nanomechanical properties under nitrogen deprivation

Although no morphological changes were observed, starved *P. kessleri* experienced a 60% decrease in Young's modulus (from 1320.7 ± 415.1 kPa, aligned with other values in the literature for *P. kessleri* (Passucci et al. 2024), to 535.8 ± 346.5 kPa) while keeping comparable roughness values (1.3 ± 0.5 nm in regular cells and 1.9 ± 1.4 nm in the starved ones). This mechanical softening as a stress response has already been reported for other microalgae (Novosel et al. 2022a, b; Demir-Yilmaz et al. 2023), and indicates that nitrogen deprivation altered the mechanical architecture of the cell wall without affecting its thickness or surface topology.

Considering that both cell types underwent freezing for storage and subsequent thawing for analysis, it could be inferred that the differences between roughness values, despite not being statistically significant, could be influenced by this variable: freezing can affect microalgal cell properties by inducing partial or total disruption or other forms of cell damage (Prieto-Guevara et al. 2023; Zurita et al. 2025) that can contribute to an increase in cell roughness (Shu et al. 2017). Interestingly, both cell types showed roughness values consistent with fresh-sample literature on *P. kessleri* (Passucci et al. 2024) and other green microalgae (Demir et al. 2020; Demir-Yilmaz et al. 2023), suggesting minimal freeze–thaw effects. Hence, the lower roughness value for regular cells may stem from differences in growth conditions. However, freeze–thaw effects cannot be fully discarded, as the interaction between average Young's modulus and average roughness was statistically significant in starved cells, revealing that softer cells had rougher surfaces ($\rho = -0.77$, $p = 0.001$). The cell debris in Fig. 1 points to this lower mechanical resistance in starved cells, while the per-cell masses indicate, as discussed in "Biochemical and per-cell mass response to nitrogen deprivation" that the freeze–thaw effect was not that extensive, so this correlation could mean that nutritional stress triggers cell wall degradation processes as well as a synergistic effect between starvation-induced cell wall weakening and freeze–thaw damage, creating rougher surface areas that lead to reduced mechanical integrity. While regular cells did not show this correlation, they had a negative correlation between cell diameter and Young's modulus ($\rho = -0.70$, $p = 0.003$), and also a negative correlation between cell height and Young's modulus close to statistical significance ($\rho = -0.44$, $p = 0.085$). These interactions mean that smaller cells showed increased rigidity, which is a size-deformability relationship that has already been documented in other works (Liang et al. 2022).

As highlighted in the introduction of this work, very few articles have evaluated the physiological response of microalgal cells to stressors using AFM, and even fewer have specifically addressed cell roughness. For example, the work by Novosel et al. (2022a) reported an increase in the average cell roughness and a general softening with increasing culture temperature in *Dunaliella tertiolecta*, *Tetraselmis suecica* and *Cylindrotheca closterium*

(12, 18 and 30ºC), although the softening degree was species-dependent. In another work with these three microalgae, Novosel et al. (2022b) noted that the Young's modulus of the three species increased when decreasing the salinity of the medium. Demir-Yilmaz et al. (2023) also explored salinity stress, but applied to *C. vulgaris* to increase lipid productivity. They found no significant differences in roughness across exponential and stationary growth phases as well as under salinity-stress conditions to increase lipid productivity. Still, cells exposed to salinity stress were remarkably softer than those in stationary phase grown under regular conditions. Roughness stability was attributed to a constant composition of the polysaccharidic fraction of the cell wall. As the cell wall composition was stable, cell softening was ascribed to a loss of turgor pressure derived from osmotic stress. The nanomechanics of *C. vulgaris* were also studied by Duval et al. (2023), but this time to understand the impact of culture growth phase and lysozyme treatment. Cells softened upon culture ageing and lost mechanical homogeneity after lysozyme exposure. Conversely, Yap et al. (2016) reported an increase in cell stiffness as a response to nitrogen deprivation: nitrogen-deprived *Chlorococcum* sp. cells had Young's modulus that were 30% greater than their nitrogen-repleted counterparts.

Given that different microalgae species respond differently to various abiotic stressors, it can be concluded that the impact of nitrogen deprivation is both species- and stressor-specific. In the case of *P. kessleri*, these results indicate that nitrogen deprivation not only induces compositional changes, but alters the mechanical architecture of the cell wall without affecting its morphological features. This observation suggests cell wall remodelling via cross-linking changes or cell wall polymer reorganisation, which may have induced the observed mechanical softening without a thickening-driven response.

Implications for freeze–thaw handling and third-generation biorefineries

All samples in this study underwent freezing for storage and subsequent thawing for analysis, a protocol that is often used within industrial contexts to preserve and transport microalgal biomass. Considering this, the fact that comparative trends in nanomechanical properties remained discernible despite this handling is significant in practical terms. As previously discussed, roughness values were consistent with the fresh-sample literature (Demir et al. 2020; Demir-Yilmaz et al. 2023; Passucci et al. 2024), suggesting that freeze–thaw did not fundamentally alter surface topology at the population level. Still, cell debris was observed within the starved batches while the per-cell mass was not significantly altered, indicating that this fragilisation was not extensive enough to cause measurable biomass loss at the population level, but rather affected individual cells that were already structurally compromised. This nuanced picture, in which freeze–thaw does not invalidate comparative trends but may amplify starvation-induced fragility in vulnerable cells, has important handling implications: while starved biomass has some processing advantages, like higher lipid content and lower Young's modulus, it may require gentler preservation protocols to minimise cell lysis during storage and transport. Future experimental work should accordingly discern the actual impact of freeze–thaw on the recorded nanomechanical properties by comparing fresh and frozen biomass, while cell walls should be characterised to evaluate eventual starvation-derived compositional changes through glycomic and proteomic analyses.

From a biotechnological perspective, the findings of the present work reveal a dual advantage of nitrogen deprivation in microalgal biorefineries. Beyond the well-known increase in lipid content in *P. kessleri* under such conditions (Taleb et al. 2016, 2018; Kandilian et al. 2019; Heredia et al. 2021), the observed reduction in cell wall rigidity (60% decrease in Young's modulus) represents a significant process optimisation opportunity. From a mechanistic perspective, a lower Young's modulus translates into lower resistance to deformation and fracture, which is expected to lower the critical stress required for mechanical disruption. Hence, softer cell walls facilitate mechanical cell disruption, potentially reducing energy requirements and processing costs in downstream lipid extraction for biofuel production (Duval et al. 2023). The exact energy and financial savings will depend on the specific disruption method used (Lee et al. 2012, 2013), but given that downstream processing accounts for around 50% of the microalgae biorefinery costs (Ruiz et al. 2016; Lam et al. 2018), even moderate improvements in energy efficiency could significantly improve its economic viability. Together, these two factors position starved *P. kessleri* as a promising feedstock for biofuel production, combining high lipid yields with lower processing costs for improved biorefinery economics.

Conclusions

This work evaluated the impact of nitrogen deprivation on *P. kessleri*, a freshwater microalga attractive for biofuel applications when cultivated under such stress conditions, by integrating biochemical characterisation with multi-scale morphological and nanomechanical analyses.

Nitrogen deprivation induced the expected metabolic shift (lipid accumulation and protein depletion) while the per-cell mass, external morphology (cell diameter and height), internal morphology (cell wall thickness) and

surface roughness remained stable. In contrast, starved cells had a 60% reduction in Young's modulus, indicating that nitrogen deprivation reshaped the mechanical architecture of the cell wall independently of its size, thickness or surface topology. This dissociation between morphology and nanomechanics suggests either limited morphological plasticity in this species, a predominantly compositional stress response, or that stress conditions were not severe enough to trigger morphological adaptations.

Although biomass freezing and subsequent thawing for analysis may have affected absolute mechanical values, roughness values in both conditions were consistent with those reported for fresh *P. kessleri* cells, supporting the comparative trends. These results indicate that nitrogen deprivation preconditions the structural integrity of the biomass, potentially affecting its susceptibility to mechanical disruption. This point is particularly relevant to realistic processing scenarios, where biomass storage and transport frequently involve freezing.

By introducing nanomechanical descriptors as complementary metrics to conventional biochemical analyses, this work supports the integration of AFM-based mechanical characterisation into microalgae biorefinery research as a tool for guiding biomass handling, disruption, and conversion strategies.

Supplementary Information The online version contains supplementary material available at https://doi.org/10.1007/s10811-026-04012-6.

Acknowledgements The authors of the URV are recognised by the Comissionat per a Universitats i Recerca del DIUE de la Generalitat de Catalunya (2017-SGR-396). The authors also thank the microscopy team from the Scientific & Technical Resources Service of Universitat Rovira i Virgili, Mariana, Èric, Rita, Mercè and Núria for their support.

Author contributions AZ: Conceptualisation, Data Curation, Formal analysis, Investigation, Methodology, Validation, Visualisation, Writing—Original Draft, Writing—Review & Editing; SS: Data Curation, Formal analysis, Investigation, Methodology, Validation, Visualisation; JPri: Resources, Formal analysis; JPru: Resources, Formal analysis; MT: Resources, Formal analysis; ET: Data curation, Funding acquisition, Methodology, Project administration, Resources; CF-D: Data Curation, Formal analysis, Investigation, Methodology, Validation, Visualisation, Resources, Supervision; CB: Conceptualisation, Data Curation, Funding acquisition, Methodology, Project administration, Supervision, Validation, Visualisation, Writing—Review & Editing.

Funding Open Access funding provided thanks to the CRUE-CSIC agreement with Springer Nature. • The funding of this work came from the COCPIT Project (COCPIT—Scalable solutions Optimisation and decision tool Creation for low impact SAF Production chain from lipid-rich microalgae strain) 4-year Horizon Europe Research and Innovation Programme under Grant Agreement No. 101122101.

• The predoctoral position of Alba Zurita was funded by the European Union NextGenerationEU, the SEPE and the URV (2022PMF-INV-09).

• Co-founding of this work was supported by the Universitat Rovira i Virgili (2022PFR-URV-25).

Data availability Data and material will be made available on reasonable request.

Declarations

Competing interests The authors declare no competing interests.

Open Access This article is licensed under a Creative Commons Attribution 4.0 International License, which permits use, sharing, adaptation, distribution and reproduction in any medium or format, as long as you give appropriate credit to the original author(s) and the source, provide a link to the Creative Commons licence, and indicate if changes were made. The images or other third party material in this article are included in the article's Creative Commons licence, unless indicated otherwise in a credit line to the material. If material is not included in the article's Creative Commons licence and your intended use is not permitted by statutory regulation or exceeds the permitted use, you will need to obtain permission directly from the copyright holder. To view a copy of this licence, visit http://creativecommons.org/licenses/by/4.0/.

References

Abreu L, Borges L, Marangoni J, Abreu PC (2012) Cryopreservation of some useful microalgae species for biotechnological exploitation. J Appl Phycol 24:1579–1588

American Public Health Association (APHA), American Water Works Association (AWWA), Water Environment Federation (WEF) (2012) Standard Methods for the Examination of Water and Wastewater, 22nd edn. Water Works Association, Washington DC

Bautista-Chamizo E, Sendra M, Cid A, Seoane M, de Orte MR, Riba I (2018) Will temperature and salinity changes exacerbate the effects of seawater acidification on the marine microalga *Phaeodactylum tricornutum*? Sci Total Environ 634:87–94

Beacham TA, Bradley C, White DA, Bond P, Ali ST (2014) Lipid productivity and cell wall ultrastructure of six strains of *Nannochloropsis*: implications for biofuel production and downstream processing. Algal Res 6:64–69

Binnig G, Quate CF, Gerber C (1986) Atomic force microscope. Phys Rev Lett 56:930

Bligh EG, Dyer WJ (1959) A rapid method of total lipid extraction and purification. Can J Biochem Physiol 37:911–917

Breuer G, Lamers PP, Martens DE, Draaisma RB, Wijffels RH (2012) The impact of nitrogen starvation on the dynamics of triacylglycerol accumulation in nine microalgae strains. Bioresour Technol 124:217–226

Caporgno MP, Taleb A, Olkiewicz M, Font J, Pruvost J, Legrand J, Bengoa C (2015) Microalgae cultivation in urban wastewater: nutrient removal and biomass production for biodiesel and methane. Algal Res 10:232–239

Caporgno MP, Olkiewicz M, Fortuny A, Stüber F, Fabregat A, Font J, Pruvost J, Lepine O, Legrand J, Bengoa C (2016) Evaluation of different strategies to produce biofuels from *Nannochloropsis oculata* and *Chlorella vulgaris*. Fuel Process Technol 144:132–138

Cappella B, Dietler G (1999) Force-distance curves by atomic force microscopy. Surf Sci Rep 34:5–104

Chokshi K, Pancha I, Ghosh A, Mishra S (2017) Nitrogen starvation-induced cellular crosstalk of ROS-scavenging antioxidants and phytohormone enhanced the biofuel potential of green microalga *Acutodesmus dimorphus*. Biotechnol Biofuels 10:60

Concas A, Pisu M, Cao G (2016) A novel mathematical model to simulate the size-structured growth of microalgae strains dividing by multiple fission. Chem Eng J 287:252–268

Cvjetinovic J, Luchkin SY, Statnik ES, Davidovich NA, Somov PA, Salimon AI, Korsunsky AM, Gorin DA (2023) Revealing the static and dynamic nanomechanical properties of diatom frustules - nature's glass lace. Sci Rep 13:5518

da Silva VB, Moreira JB, de Morais MG, Costa JAV (2016) Microalgae as a new source of bioactive compounds in food supplements. Curr Opin Food Sci 7:73–77

Dasan YK, Lam MK, Yusup S, Lim JW, Lee KT (2019) Life cycle evaluation of microalgae biofuels production: effect of cultivation system on energy, carbon emission and cost balance analysis. Sci Total Environ 688:112–128

Demir I, Blockx J, Dague E, Guiraud P, Thielemans W, Muylaert K, Formosa-Dague C (2020) Nanoscale evidence unravels microalgae flocculation mechanism induced by chitosan. ACS Appl Bio Mater 3:8446–8459

Demir-Yilmaz I, Guiraud P, Formosa-Dague C (2021) The contribution of Atomic Force Microscopy (AFM) in microalgae studies: A review. Algal Res 60:102506

Demir-Yilmaz I, Schiavone M, Esvan J, Guiraud P, Formosa-Dague C (2023) Combining AFM, XPS and chemical hydrolysis to understand the complexity and dynamics of *C. vulgaris* cell wall composition and architecture. Algal Res 72:103102

Dubois M, Gilles KA, Hamilton JK, Rebers PA, Smith F (1956) Colorimetric method for determination of sugars and related substances. Anal Chem 28:350–356

Duval JF, Razafitianamaharavo A, Bihannic I, Offroy M, Lesniewska N, Sohm B, Le Cordier H, Mustin C, Pagnout C, Beaussart A (2023) New insights into the effects of growth phase and enzymatic treatment on the cell-wall properties of *Chlorella vulgaris* microalgae. Algal Res 69:102955

Fekete G, Sebők A, Klátyik S, Varga ZI, Grósz J, Czinkota I, Székács A, Aleksza L (2024) Comparative analysis of laboratory-based and spectroscopic methods used to estimate the algal density of *Chlorella vulgaris*. Microorganisms 12:1050

Filali R, Tian H, Micheils E, Taidi B (2021) Evaluation of the growth performance of microalgae based on fine pH changes. Austin J Biotechnol Bioeng 8:1109

Godon C, Teulon JM, Odorico M, Basset C, Meillan M, Vellutini L, Chen SWW, Pellequer JL (2017) Conditions to minimize soft single biomolecule deformation when imaging with atomic force microscopy. J Struct Biol 197:322–329

González-Hourcade M, Fernando D, Gentili FG (2023) Morphological and cellular organization of green microalgae to cope with cold stress in subarctic environment. Algal Res 75:103254

Halim R, Hill DR, Hanssen E, Webley PA, Martin GJ (2019) Thermally coupled dark-anoxia incubation: a platform technology to induce auto-fermentation and thus cell-wall thinning in both nitrogen-replete and nitrogen-deplete *Nannochloropsis* slurries. Bioresour Technol 290:121769

Havlik I, Reardon KF, Ünal M, Lindner P, Prediger A, Babitzky A, Beutel S, Scheper T (2013) Monitoring of microalgal cultivations with on-line, flow-through microscopy. Algal Res 2:253–257

Heredia V, Gonçalves O, Marchal L, Pruvost J (2021) Producing energy-rich microalgae biomass for liquid biofuels: influence of strain selection and culture conditions. Energies 14:1246

Hsu WH, Chien YH, Tsai HY (2020) Experimental and modeling analysis of the cell-wall fracture of *Nannochloropsis oculata*. J Mech 36:789–797

Hu W (2014) Dry weight and cell density of individual algal and cyanobacterial cells for algae research and development. MSc Thesis, University of Missouri-Columbia, USA

Hutter JL, Bechhoefer J (1993) Calibration of atomic-force microscope tips. Rev Sci Instrum 64:1868–1873

Jeong SW, Nam SW, HwangBo K, Jeong WJ, Jeong BR, Chang YK, Park YI (2017) Transcriptional regulation of cellulose biosynthesis during the early phase of nitrogen deprivation in *Nannochloropsis salina*. Sci Rep 7:5264

Juárez ÁB, Vélez CG, Iñiguez AR, Martínez DE, Rodríguez MC, Vigna MS, del Carmen Rios de Molina M (2011) A *Parachlorella kessleri* (Trebouxiophyceae, Chlorophyta) strain from an extremely acidic geothermal pond in Argentina. Phycologia 50:413–421

Kandilian R, Taleb A, Heredia V, Cogne G, Pruvost J (2019) Effect of light absorption rate and nitrate concentration on TAG accumulation and productivity of *Parachlorella kessleri* cultures grown in chemostat mode. Algal Res 39:101442

Kautsky H, Hirsch A (1931) Neue Versuche zur Kohlensäureassimilation. Naturwissenschaften 19:964

Kemel S, Marchal L, Habiba WN, Marec H, Drouin D, Gonçalves O, Pruvost J (2025) Investigation of the colony size effect on light access and growth of the colonial microalga *Botryococcus braunii* in photobioreactor. Algal Res 90:104176

Krienitz L, Hegewald EH, Hepperle D, Huss VA, Rohr T, Wolf M (2004) Phylogenetic relationship of *Chlorella* and *Parachlorella* gen. nov. (Chlorophyta, Trebouxiophyceae). Phycologia 43:529–542

Lam GT, Vermuë MH, Eppink MHM, Wijffels RH, Van Den Berg C (2018) Multi-product microalgae biorefineries: from concept towards reality. Trends Biotechnol 36:216–227

Lee JY, Yoo C, Jun SY, Ahn CY, Oh HM (2010) Comparison of several methods for effective lipid extraction from microalgae. Bioresour Technol 101:S75–S77

Lee AK, Lewis DM, Ashman PJ (2012) Disruption of microalgal cells for the extraction of lipids for biofuels: processes and specific energy requirements. Biomass Bioenergy 46:89–101

Lee AK, Lewis DM, Ashman PJ (2013) Force and energy requirement for microalgal cell disruption: an atomic force microscope evaluation. Bioresour Technol 128:199–206

Liang M, Zhong J, Ai Y (2022) A systematic study of size correlation and Young's modulus sensitivity for cellular mechanical phenotyping by microfluidic approaches. Adv Health Mater 11:2200628

Liu S, Rouquié C, Lavenant L, Frappart M, Couallier E (2022) Coupling bead-milling and microfiltration for the recovery of lipids and proteins from *Parachlorella kessleri*: impact of the cell disruption conditions on the separation performances. Sep Purif Technol 287:120570

Lowry OH, Rosebrough NJ, Farr AL, Randall RJ (1951) Protein measurement with the Folin phenol reagent. J Biol Chem 193:265–275

Mata TM, Martins AA, Caetano NS (2010) Microalgae for biodiesel production and other applications: a review. Renew Sustain Energ Rev 14:217–232

Mišić Radić T, Vukosav P, Komazec B, Formosa-Dague C, Domazet Jurašin D, Peharec Štefanić P, Čačović A, Juraić K, Ivošević DeNardis N (2022) Nanoplastic-induced nanostructural, nanomechanical, and antioxidant response of marine diatom *Cylindrotheca closterium*. Water 14:2163

Mišić Radić T, Vukosav P, Čačković A, Dulebo A (2023) Insights into the morphology and surface properties of microalgae at the nanoscale by Atomic Force Microscopy (AFM): a review. Water 15:1983

Novosel N, Mišić Radić T, Zemla J, Lekka M, Čačković A, Kasum D, Legović T, Žutinić P, Gligora Udovič M, Ivošević DeNardis N (2022a) Temperature-induced response in algal cell surface properties and behaviour: an experimental approach. J Appl Phycol 34:243–259

Novosel N, Mišić Radić T, Levak Zorinc M, Zemla J, Lekka M, Vrana I, Gašparović B, Horvat L, Kasum D, Legović T, Žutinić P, Gligora Udovič M, Ivošević DeNardis N (2022b) Salinity-induced chemical, mechanical, and behavioral changes in marine microalgae. J Appl Phycol 34:1293–1309

Olkiewicz M, Caporgno MP, Font J, Legrand J, Lepine O, Plechkova NV, Pruvost J, Seddon KR, Bengoa C (2015) A novel recovery

process for lipids from microalgæ for biodiesel production using a hydrated phosphonium ionic liquid. Green Chem 17:2813–2824
Pancha I, Chokshi K, George B, Ghosh T, Paliwal C, Maurya R, Mishra S (2014) Nitrogen stress triggered biochemical and morphological changes in the microalgae *Scenedesmus sp.* CCNM 1077. Bioresour Technol 156:146–154
Passucci V, Thomas-Chemin O, Dib O, Assaf AA, Durand MJ, Dague E, Areco MM, Formosa-Dague C (2024) Investigating the role of extracellular polymeric substances produced by *Parachlorella kessleri* in Zn(II) bioremediation using atomic force microscopy. Environ Pollut 363:125082
Pietuch A, Janshoff A (2013) Mechanics of spreading cells probed by atomic force microscopy. Open Biol 3:130084
Prieto-Guevara M, Alarcón-Furnieles J, Jiménez-Velásquez C, Hernández-Julio Y, Espinosa-Araujo J, Atencio-García V (2023) Cryopreservation of the microalgae *Scenedesmus* sp. Cells 12:562
Pruvost J, Van Vooren G, Cogne G, Legrand J (2009) Investigation of biomass and lipids production with *Neochloris oleoabundans* in photobioreactor. Bioresour Technol 100:5988–5995
Pruvost J, Van Vooren G, Le Gouic B, Couzinet-Mossion A, Legrand J (2011) Systematic investigation of biomass and lipid productivity by microalgae in photobioreactors for biodiesel application. Bioresour Technol 102:150–158
Ran W, Wang H, Liu Y, Qi M, Xiang Q, Yao C, Zhang Y, Lan X (2019) Storage of starch and lipids in microalgae: biosynthesis and manipulation by nutrients. Bioresour Technol 291:121894
Raven JA, Beardall J (2006) Chlorophyll fluorescence and ecophysiology: seeing red? New Phytol 169:449–451
Rheinlaender J, Dimitracopoulos A, Wallmeyer B, Kronenberg NM, Chalut KJ, Gather MC, Betz T, Charras G, Franze K (2020) Cortical cell stiffness is independent of substrate mechanics. Nature Materials 19:1019–1025
Rivas-Navia D, CheikhWafa J, Zurita A, Torrens E, Bengoa C (2025) Design of a Ɛ-caprolactam-based ionic liquids for the extraction of lipids from starved *Parachlorella kessleri* microalgae for sustainable aviation fuels (SAF). Algal Res 92:104369
Rivera EC, Montalescot V, Viau M, Drouin D, Bourseau P, Frappart M, Monteux C, Couallier E (2018) Mechanical cell disruption of *Parachlorella kessleri* microalgae: impact on lipid fraction composition. Bioresour Technol 256:77–85
Rodolfi L, Chini Zittelli G, Bassi N, Padovani G, Biondi N, Bonini G, Tredici MR (2009) Microalgae for oil: strain selection, induction of lipid synthesis and outdoor mass cultivation in a low-cost photobioreactor. Biotechnol Bioeng 102:100–112
Roncaglia B, Papini A, Chini Zittelli G, Rodolfi L, Tredici MR (2021) Cell wall and organelle modifications during nitrogen starvation in *Nannochloropsis oceanica* F&M-M24. J Appl Phycol 33:2069–2080
Ruiz J, Olivieri G, De Vree J, Bosma R, Willems P, Reith JH, Eppink MHM, Kleinegris DMM, Wijffels R, Barbosa MJ (2016) Towards industrial products from microalgae. Energy Environ Sci 9:3036–3043
Shivakumar S, Serlini N, Esteves SM, Miros S, Halim R (2024) Cell walls of lipid-rich microalgae: a comprehensive review on characterisation, ultrastructure, and enzymatic disruption. Fermentation 10:608
Shu W, Zhao L, Hou S, Yu QJ, Tan S, Yin P (2017) Toxic effect on the membrane system and cell proliferation of *Prorocentrum donghaiense* caused by the novel algicidal fungus *Talaromyces purpurogenus* YL13. J Appl Phycol 29:275–284
Siddiki SYA, Mofijur M, Kumar PS, Ahmed SF, Inayat A, Kusumo F, Badruddin IA, Khan TMY, Nghiem LD, Ong HC, Mahlia TMI (2022) Microalgae biomass as a sustainable source for biofuel, biochemical and biobased value-added products: an integrated biorefinery concept. Fuel 307:121782
Sneddon IN (1965) The relation between load and penetration in the axisymmetric Boussinesq problem for a punch of arbitrary profile. Int J Eng Sci 3:47–57
Spain O, Funk C (2022) Detailed characterization of the cell wall structure and composition of Nordic green microalgae. J Agric Food Chem 70:9711–9721
Spolaore P, Joannis-Cassan C, Duran E, Isambert A (2006) Commercial applications of microalgae. J Biosci Bioeng 101:87–96
Sun H, Zhao W, Mao X, Li Y, Wu T, Chen F (2018) High-value biomass from microalgae production platforms: strategies and progress based on carbon metabolism and energy conversion. Biotechnol Biofuels 11:1–23
Takeda H (1991) Sugar composition of the cell wall and the taxonomy of *Chlorella* (Chlorophyceae). J Phycol 27:224–232
Taleb A, Kandilian R, Touchard R, Montalescot V, Rinaldi T, Taha S, Takache H, Marchal L, Legrand J, Pruvost J (2016) Screening of freshwater and seawater microalgae strains in fully controlled photobioreactors for biodiesel production. Bioresour Technol 218:480–490
Taleb A, Legrand J, Takache H, Taha S, Pruvost J (2018) Investigation of lipid production by nitrogen-starved *Parachlorella kessleri* under continuous illumination and day/night cycles for biodiesel application. J Appl Phycol 30:761–772
Tibbetts SM, Milley JE, Lall SP (2015) Chemical composition and nutritional properties of freshwater and marine microalgal biomass cultured in photobioreactors. J Appl Phycol 27:1109–1119
Villafaña-López L, Rivera EC, Liu S, Couallier E, Frappart M (2019) Shear-enhanced membrane filtration of model and real microalgae extracts for lipids recovery in biorefinery context. Bioresour Technol 288:121539
Wadu-Mesthrige K, Amro NA, Garno JC, Cruchon-Dupeyrat S, Liu GY (2001) Contact resonance imaging—a simple approach to improve the resolution of AFM for biological and polymeric materials. Appl Surf Sci 175:391–398
Wang ZT, Ullrich N, Joo S, Waffenschmidt S, Goodenough U (2009) Algal lipid bodies: stress induction, purification, and biochemical characterization in wild-type and starchless *Chlamydomonas reinhardtii*. Eukaryot Cell 8:1856–1868
Yap BH, Crawford SA, Dagastine RR, Scales PJ, Martin GJ (2016) Nitrogen deprivation of microalgae: effect on cell size, cell wall thickness, cell strength, and resistance to mechanical disruption. J Ind Microbiol Biotechnol 43:1671–1680
Zhang R, Grimi N, Marchal L, Vorobiev E (2019a) Application of high-voltage electrical discharges and high-pressure homogenization for recovery of intracellular compounds from microalgae *Parachlorella kessleri*. Bioprocess Biosyst Eng 42:29–36
Zhang R, Grimi N, Marchal L, Lebovka N, Vorobiev E (2019b) Effect of ultrasonication, high pressure homogenization and their combination on efficiency of extraction of bio-molecules from microalgae *Parachlorella kessleri*. Algal Res 40:101524
Zurita A, Mateo-Sanz JM, Legrand J, Pruvost J, Hernández-Malo R, Muñoz-Domenech M, Torrens E, Bengoa C (2025) Optimization of biomolecule extraction from *Spirulina platensis* with [bmim][Cl]. Algal Res 86:103909
Zurita A, Sebastiano S, Dupré C, Prieto J, Torrens E, Formosa-Dague C, Bengoa C (2026) From contamination to valorisation: a case study assessing culture contamination effect on the biofuel potential and nanomechanical properties of *Parachlorella kessleri*. Biotechnol Biofuels Bioprod. https://doi.org/10.1186/s13068-026-02789-9

Publisher's Note Springer Nature remains neutral with regard to jurisdictional claims in published maps and institutional affiliations.